DRAFT VERSION AUGUST 19, 2016
Preprint typeset using LaTeX style emulateapj v. 5/2/11

arXiv:1608.05320v1 [astro-ph.HE] 18 Aug 2016

ASYMMETRIC CORE-COLLAPSE OF RAPIDLY-ROTATING MASSIVE STAR

AVISHAI GILKIS
Department of Physics, Technion – Israel Institute of Technology, Haifa 32000, Israel; agilkis@technion.ac.il
Draft version August 19, 2016

ABSTRACT

Non-axisymmetric features are found in the core-collapse of a rapidly-rotating massive star, which may have important implications for magnetic field amplification and production of a bipolar outflow that can explode the star, as well as for *r*-process nucleosynthesis and natal kicks. The collapse of an evolved rapidly-rotating $M_{\rm ZAMS} = 54 M_\odot$ star is followed in three-dimensional hydrodynamic simulations using the FLASH code with neutrino leakage. A rotating proto-neutron star (PNS) forms with a non-zero linear velocity. This process might contribute to the natal kick of the remnant compact object. The PNS is surrounded by a turbulent medium, where high shearing is likely to amplify magnetic fields, which in turn can drive a bipolar outflow. Neutron-rich material in the PNS vicinity may induce strong *r*-process nucleosynthesis. The rapidly-rotating PNS possesses a rotational energy of $E_{\rm rot} \gtrsim 10^{52}$ erg, some of which may possibly be deposited later on in the SN ejecta through a magnetar spin down process. These processes may be important for rare supernovae generated by rapidly-rotating progenitors, even though a successful explosion is not simulated in the present study.

Key words: stars: massive — stars: rotation — supernovae: general

1. INTRODUCTION

Most core-collapse supernovae (CCSNe) are observed to have explosion energies around $E_{\rm expl} \approx 10^{51}$ erg $\equiv 1$ foe (e.g., Kasen & Woosley 2009; Drout et al. 2011). In recent years, several super-luminous supernovae (SLSNe) have been observed (e.g., Quimby et al. 2011, 2013; Gal-Yam 2012; Prajs et al. 2016). Some of these are Type IIn SNe, and their extreme luminosity is generally attributed to the collision of the ejecta with circumstellar material (e.g., Ofek et al. 2007; Rest et al. 2011) ejected in a pre-explosion outburst (PEO). The physical mechanism and the relative rarity of PEOs are yet to be fully-understood (for recent ideas see Quataert & Shiode 2012; Shiode & Quataert 2014; Mcley & Soker 2014; Soker & Gilkis 2016).

The case of hydrogen-poor SLSNe (Type I SLSNe, or SLSNe-I) is more complicated, with extreme examples such as SN 2010ay (Sanders et al. 2012) and ASASSN-15lh (Dong et al. 2016). A variety of proposed mechanisms includes interaction with pre-explosion ejecta from pulsational pair-instability (Chatzopoulos & Wheeler 2012), injection of energy from a millisecond magnetar (e.g., Kasen & Bildsten 2010; Inserra et al. 2013; Kasen et al. 2016; Sukhbold & Woosley 2016), the transition of a neutron star (NS) into a quark star (quark novae; Ouyed et al. 2015, 2016) and energy deposition by bipolar jets (Gilkis et al. 2016). A combination of circumstellar interaction and magnetar spin-down has been proposed as well (Chatzopoulos et al. 2016), and magnetar birth may also be accompanied by jets (Soker 2016).

A clue for the operating mechanism of these SLSNe-I may be gleamed from their apparent connection to long-duration gamma-ray bursts (LGRBs). The hosts of both types of transients are low-luminosity and low-metallicity galaxies with high star-formation rates (Lunnan et al. 2014), although some differences are observed (Leloudas et al. 2015; Angus et al. 2016). There may be a common process leading to these separate phenomena. Metzger et al. (2015), for example, suggest that magnetars are the powering mechanism in both SLSNe-I and LGRBs. Another possibility is that jets launched from an accretion disk around a compact object power these events (Milosavljević et al. 2012; Dexter & Kasen 2013).

The mechanisms mentioned above call for a rapid rotation of the progenitor star, and it is important to understand how this can be accommodated by the evolution of massive stars (see review by Langer 2012). The rarity of SLSNe-I and LGRBs may be compatible with the requirement for high rotation, as stellar evolution models predict that massive stars will lose most of their angular momentum (Meynet & Maeder 2000). Specific binary interactions (e.g., Izzard et al. 2004; Podsiadlowski et al. 2004; Fryer & Heger 2005; Cantiello et al. 2007; Yoon et al. 2010; de Mink et al. 2013) or chemically homogeneous stellar evolution (Yoon & Langer 2005; Woosley & Heger 2006; Martins et al. 2013; Mandel & de Mink 2016; Song et al. 2016) may be required to supply the high rotation needed for extreme explosion scenarios.

Recent three-dimensional hydrodynamic core-collapse simulations of rotating stars have yielded intriguing results. Nakamura et al. (2014) and Takiwaki et al. (2016) showed a preferred explosion direction *perpendicular* to the rotation axis. Mösta et al. (2014) preformed three-dimensional magnetorotational simulations of core-collapse, finding a phenomenon of magnetically-inflated asymmetric lobes. Other studies focused on the properties of gravitational waves expected from the collapse of a rotating star (Ott et al. 2007; Kuroda et al. 2014). Iwakami et al. (2009) imposed rotation after core-collapse, and their findings suggest that rotation can affect the standing accretion-shock instability (SASI; e.g., Blondin et al. 2003; Blondin & Mezzacappa 2007; Fernández 2010).

To advance the understanding of the possible origin and mechanism of SLSNe-I, atypical progenitor stars should be considered, such as those with extremely rapid rotation rates, or very high mass. In the present study I explore the properties of the post-collapse flow in a very massive rapidly-rotating star. Three-dimensional hydrodynamic simulation of the stellar collapse are performed, including deleptonization and a

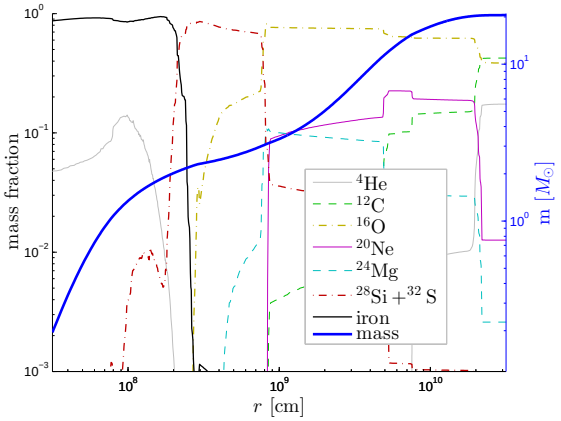

FIG. 1.— Detailed composition for the stellar model just before core-collapse of a rotating $M_{\rm ZAMS} = 54 M_\odot$ star with metallicity of $Z = 0.014$, and magnetic braking neglected. The stellar parameters at this stage are stellar mass of $M = 20.5 M_\odot$, effective temperature of $T = 2.4 \times 10^5 K$, photospheric radius of $R = 0.55 R_\odot$ and luminosity of $L = 9 \times 10^5 L_\odot$.

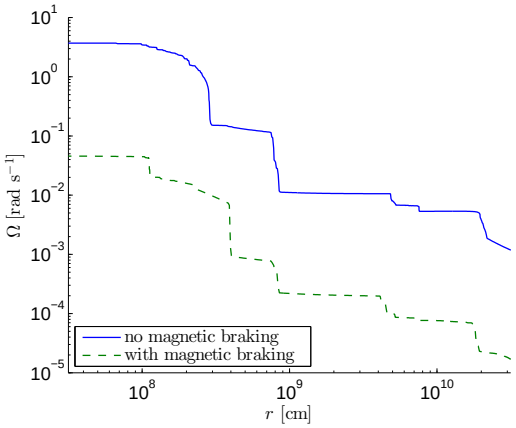

FIG. 2.— Comparing angular velocity of two stellar models with same initial conditions, where in one model magnetic braking is included and in the other it is neglected. r is the shell radius (distance from the center of the star), and Ω is assumed constant within each shell.

neutrino leakage scheme for heating and cooling. For comparison, a slowly-rotating case is simulated as well. In section 2 I describe the numerical setup and method. The flow structure of the collapse and implications for CCSNe are presented in section 3. I summarize in section 4.

2. NUMERICAL SETUP

2.1. *Progenitor modeling*

A stellar model constructed by Modules for Experiments in Stellar Astrophysics (MESA version 7624; Paxton et al. 2011, 2013, 2015) is used, with an initial mass of $M_{\rm ZAMS} = 54 M_\odot$ and metallicity of $Z = 0.014$. Due to stellar winds calculated here with the so-called 'Dutch' scheme (e.g., Nugis & Lamers 2000; Vink et al. 2001) the final mass is $20.5 M_\odot$. The initial rotation is 0.55 of the break-up value, which corresponds to a surface rotation velocity of $v_{\rm ZAMS} = 360$ km s^{-1}. Magnetic braking by the Spruit-Tayler dynamo (Spruit 2002) is neglected, effectively resulting in a high core rotation which might not be expected in a single-star model. At this stage, the star is a Wolf-Rayet star, with an effective surface temperature of $T = 2.4 \times 10^5 K$, photospheric radius of $R = 0.55 R_\odot$ and luminosity of $L = 9 \times 10^5 L_\odot$. The detailed composition of the stellar model is shown in Figure 1.

A second stellar model is evolved with magnetic braking included. The inclusion of magnetic braking results in a core rotation lower by almost two orders of magnitude (Fig. 2). The stellar model which includes magnetic braking has a pre-collapse total rotational kinetic energy of $E_{\rm rot,slow} = 2.07 \times 10^{46}$ erg. For the case where magnetic braking was not included, the total rotational kinetic energy is $E_{\rm rot,fast} = 1.58 \times 10^{50}$ erg. The iron core of the fast rotator has a mass of $M_{\rm iron,fast} \approx 2 M_\odot$ (almost the same as with magnetic braking) and rotational kinetic energy of $E_{\rm rot,iron,fast} = 1.07 \times 10^{50}$ erg – a significant fraction of the entire rotational energy of the stellar model. The final mass, internal structure and surface properties for the two models are very similar, and the small differences in those will not be discussed.

The stellar models are followed until a core of iron-group elements forms, and then the core becomes unstable and starts to collapse. The MESA evolution is terminated when the maximal infall velocity reaches $v = 1000$ km s^{-1}. At this stage the one-dimensional profile is mapped into the three-dimensional grid of a hydrodynamic simulation, described in the next section.

2.2. *Hydrodynamic simulations*

The non-relativistic hydrodynamic equations are solved with version 4.3 of the widely-used code FLASH (Fryxell et al. 2000). Newtonian self-gravity is included employing the spherical multipole approximation of Couch et al. (2013) for solving Poisson's equation, with a multipole cutoff of $l_{\rm max} = 16$. The equation of state of Lattimer & Swesty (1991) is employed with incompressibility parameter of $K = 220$ MeV.

The density (ρ), temperature (T), electron fraction ($Y_{\rm e}$) and radial velocity (v_r) of the one-dimensional MESA profile are mapped into the three-dimensional grid. The small deformations of the one-dimensional shells due to rotation are neglected, so that the initial profiles of ρ, T, and $Y_{\rm e}$ are spherically symmetric. A non-radial velocity component is added according to the angular velocity (Fig. 2), with a constant angular velocity for each radial location, $\Omega(r)$. The added velocity component in the plane perpendicular to the rotation axis (the xz plane) is then $v_{xz} = \sqrt{x^2 + z^2}\Omega(r)$.

The three-dimensional simulation domain is a cube with edge length of 12000 km centered around the star. The mass enclosed in this domain is about $3 M_\odot$, out of the total stellar mass of $20.5 M_\odot$. For studying the early-time post-bounce flow dynamics this is sufficient. With nine levels of adaptive mesh refinement the finest resolution of the grid is 1.95 km.

2.3. *Neutrino physics*

Deleptonization of the core, approximate treatment of neutrino transport by a leakage scheme and heating by neutrinos are treated according to the methods of O'Connor & Ott (2010). The usage in the FLASH code is the implementation described in Couch & O'Connor (2014), and here only the main aspects are repeated.

Up until bounce, defined as the first time when the maximal density exceeds 2×10^{14} g cm^{-3} and the maximal entropy per nucleon is above $3 k_{\rm B}$, core deleptonization is according to a fit of the electron fraction as function of density from the 1D simulations of Liebendörfer (2005). As hypothesized by

Liebendörfer (2005), the application of the scheme to cases of fast rotation (as in the present study) should be a reasonable approximation, although this should be checked in the future. After core bounce, further deleptonization is according to the leakage scheme.

The leakage scheme interpolates between the optically thick and the optically thin regimes, where in the former neutrinos 'leak' out on a diffusion timescale, and immediately in the latter. Effective lepton and energy emission rates are obtained by interpolating between the diffusion rate and 'free' emission rate. The diffusion rates require a calculation of the local optical depth. This is done on a spherical grid of radial rays, where the computation of the optical depth by radial integration from infinity is simple, and then interpolated back to the Cartesian grid of the hydrodynamic simulation. The spherical grid has 37 polar divisions (from $\theta = 0$ to $\theta = \pi$, where θ is the angle relative to the rotation axis y) and 75 azimuthal divisions (from $\phi = 0$ to $\phi = 2\pi$, where ϕ is the angle from the x axis in the xz plane). Each ray consists of 1000 radial zones. The radial rays are uniformly spaced from $r = 0.5$ km up to $r = 150$ km, followed by a logarithmic distribution up to $r = 3000$ km.

Local neutrino heating, which is not covered by the leakage scheme described above, is added depending on the neutrino emission integrated outwards on the radial rays. This heating is then subtracted from the effective energy emission rate. The interactions taken into account in the portrayed scheme are the following. For the free emission the included interactions are electron and positron capture on protons and neutrons, respectively, as well as thermal processes. The opacity calculations include absorption of electron neutrinos on neutrons and electron antineutrinos on protons, and elastic scattering of all flavors of neutrinos on protons and neutrons. Finally, charged-current heating by absorption of electron neutrinos on neutrons and antineutrinos on protons is included. Further details can be found in O'Connor & Ott (2010), Ott et al. (2013) and Couch & O'Connor (2014), and references therein.

3. RESULTS

3.1. *Flow structure*

The two simulations were run until a post-bounce time of $t_{\rm pb} \simeq 225$ ms. The main features of interest found for the fast rotator model are not seen in the slow rotator, and the slow rotator behaves in a very similar fashion to a non-rotating progenitor. As there are extensive detailed studies of non-rotating core-collapse with a more accurate description of neutrino physics and higher resolution (e.g., Lentz et al. 2015; Melson et al. 2015; Kuroda et al. 2016; Roberts et al. 2016 for recent works; Janka 2012, Janka et al. 2016 and Müller 2016 for reviews), I will not further discuss the simulation of a slowly-rotating progenitor, except briefly in section 3.3.

Figure 3 shows the properties of the flow structure at two times after core-bounce for the rapidly-rotating model, $t_{\rm pb} = 104$ ms and $t_{\rm pb} = 224$ ms. A torus-like dense region is clearly seen surrounding the oblate proto-neutron star (PNS). Above and below the PNS are high-entropy turbulent regions. When the two 'polar holes' (one at each side of the equatorial plane) in the torus are closed, the shock waves produce high-entropy regions near the rotation axis. Figure 4 shows a close-up of the turbulent velocity field.

Figure 5 shows the radial velocity in the equatorial plane of the star. At the earlier time shown, a spiral pattern is seen, and at the later time ripples of inward and outward radial velocity surround the central region. These phenomena are strongly influenced by the self-gravity of the gas. The ratio between the gravitational time, defined as $t_{\rm G} = (G\rho)^{-1/2}$, to the dynamical time $t_{\rm dyn} = r/c_s$, is very close to unity up to around $r \approx 150-200$ km near the equatorial plane. This is the region in which the spiral pattern and ripples are seen.

At the end of the simulation, the star still experiences ongoing collapse. This can be interpreted as a failure to explode the star. However, key physical ingredients not taken into account in the simulation – magnetic fields and their amplification – may bring about a successful CCSN. I elaborate on the possible explosion and its attributes in the next sections.

3.2. *Implications for magnetic activity*

The velocity perpendicular to the meridional plane and its derivative within this plane with respect to the direction perpendicular to the initial rotation axis are presented in Figure 6 for a time of $t_{\rm pb} = 104$ ms. In Figure 6 the meridional plane is taken to be the xy plane, such that the velocity presented is in the z direction , v_z, and the derivative shown is $\frac{\partial v_z}{\partial x}$. This illustrates the strong shearing present in the turbulent flow. The regions of highest shearing are in the high entropy regions above and below the equatorial plane (Fig. 3). The shearing reaches quantitative values of $\frac{\partial v_y}{\partial x} \approx 2000\ {\rm s}^{-1}$. For comparison, the Keplerian velocity divided by the distance from the rotation axis is of an order of magnitude lower.

Mösta et al. (2015) have shown that turbulent shearing around a rapidly-rotating PNS can facilitate fast growth of magnetic fields through the magnetorotational instability. The amplified magnetic fields might then launch jets which can explode the star. I suggest that the flow structure seen in the simulation of a rapidly-rotating progenitor reported here is likewise favorable for a jet-driven explosion. This will have to be confirmed by magnetohydrodynamic simulations, which Mösta et al. (2015) show require extremely high resolution (see also Masada et al. 2015; Rembiasz et al. 2016).

3.3. *PNS formation*

The PNS is defined as the region in the simulation where the material density is above $10^{11}\ {\rm g\ cm^{-3}}$ (this definition is common in other works, e.g., Nakamura et al. 2014). The total mass, momentum, angular momentum, and moment of inertia of the PNS are calculated after core-bounce for the simulation of a rapidly-rotating progenitor, as well as for the slow rotator. The derived linear velocity is shown in Figure 7, and the total mass and effective radius are presented in Figure 8.

The slow rotator acquires a very low velocity, of $v < 10\ {\rm km\ s^{-1}}$. For the rapidly-rotating progenitor the picture is different. The x and z components of the velocity (in the plane perpendicular to the axis of rotation) of the fast rotator are highly-variable, fluctuating in a range of above $100\ {\rm km\ s^{-1}}$. At the end of the simulation, the PNS velocity in the xz plane is $v_{xz} \approx 110\ {\rm km\ s^{-1}}$. The y component of the velocity is somewhat less variable.

At the end of the simulations, the mass of the PNS for the slowly-rotating case exceeds $M_{\rm PNS} \gtrsim 2.2 M_\odot$, and is still growing. It is likely that BH formation is inevitable. For the rapid rotator the final PNS mass in the simulation is $M_{\rm PNS} \approx 1.6 M_\odot$. If the accretion is not stopped by an explosion, the PNS will continue to grow in mass, and its kick velocity will decrease. Eventually it will collapse into a BH with low or zero kick velocity. If, however, a bipolar outflow drives a successful explosion as suggested in section 3.2, the

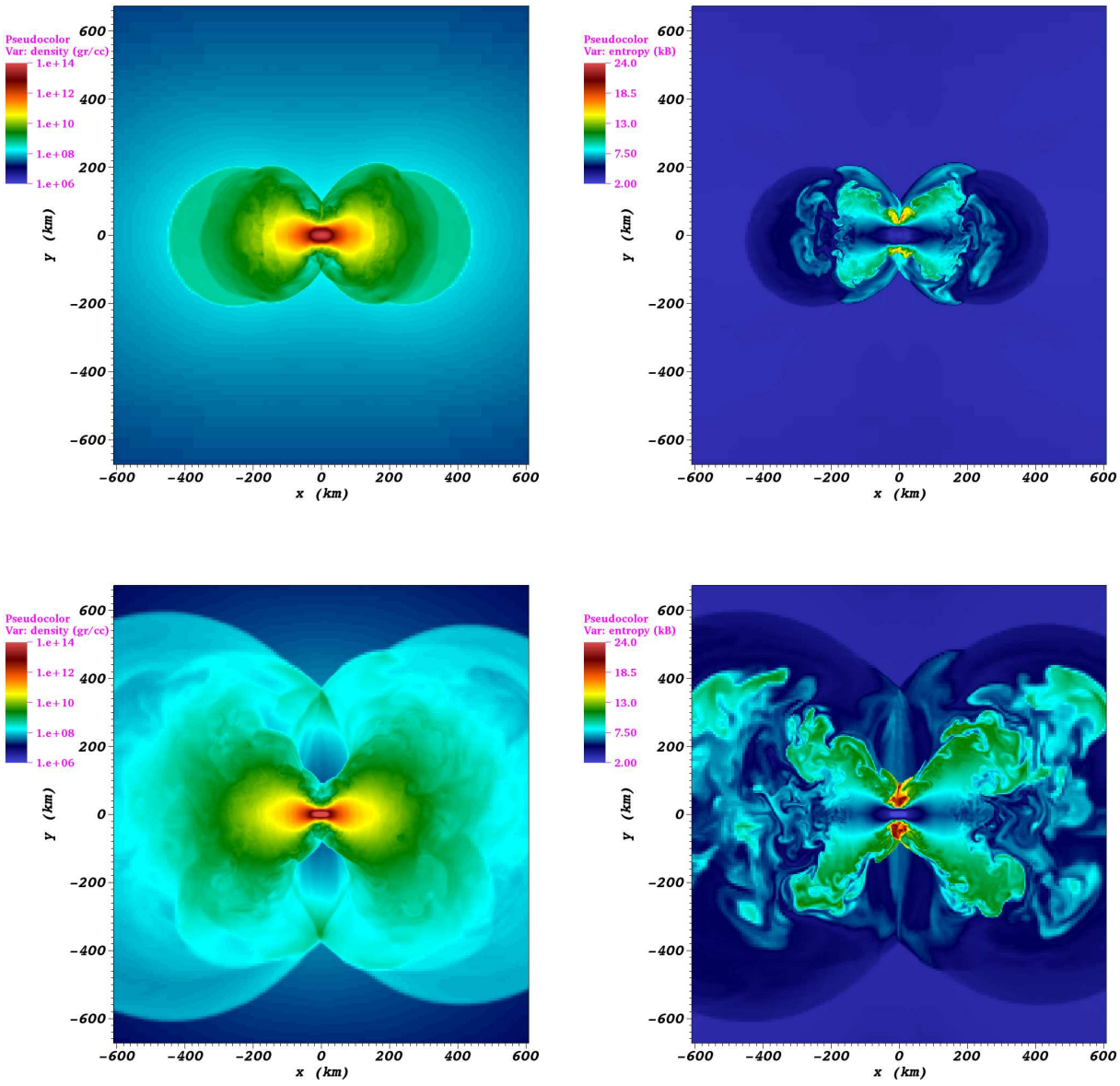

FIG. 3.— Density (left) and entropy (right) color-maps in the xy plane, where y is the axis of rotation. The density color-coding runs from $\rho = 10^6$ g cm^{-3} to $\rho = 10^{14}$ g cm^{-3}. Entropy is shown in units of $k_{\rm B}$ per nucleon. The presented times are $t_{\rm pb} = 104$ ms (top panels) and $t_{\rm pb} = 224$ ms (bottom panels).

PNS may retain its high velocity. The final kick velocity of the remnant depends on the stage at which the explosion occurs, as well as the efficiency of expelling material, and in this manner the kick velocity depends on the mass of the ejecta (Bray & Eldridge 2016). An inefficient feedback may result in continued accretion and the formation of a BH, although a higher energy SN may be the result (Gilkis et al. 2016). Still, at some point accretion onto the PNS (or BH) will stop, and a BH or NS with non-zero natal kick will emerge from the explosion. Non-zero BH kicks are favoured by recent studies (e.g., Repetto et al. 2012).

As seen in Figure 7, the kick velocity components in the equatorial plane are larger than in the direction of the rotation axis. The turbulent nature of the gas flow from which jets are conjectured to be driven may cause asymmetric mass ejection, further enhancing the kick velocity with an additional component in the y axis by the mechanism proposed by Janka (2013). An analysis by Repetto & Nelemans (2015) suggests that at least some BHs form with relatively high natal kicks (see also Mandel 2016).

Figure 9 shows the derived spin period and rotational kinetic energy of the PNS. The rotation period of the PNS for the rapidly-rotating case is $P_{\rm PNS} \approx 10$ ms just after core bounce, and decreases to $P_{\rm PNS} \approx 5$ ms by the end of the simulation. The total rotational kinetic energy grows from $E_{\rm rot} \approx 5 \times 10^{51}$ erg at very early times after bounce to $E_{\rm rot} \approx 3 \times 10^{52}$ erg near the end of the simulation. This is more than the energy required by some magnetar-driven models for SLSNe (e.g., Chen et al. 2016). The PNS in the present simulation is perhaps an early stage in the forma-

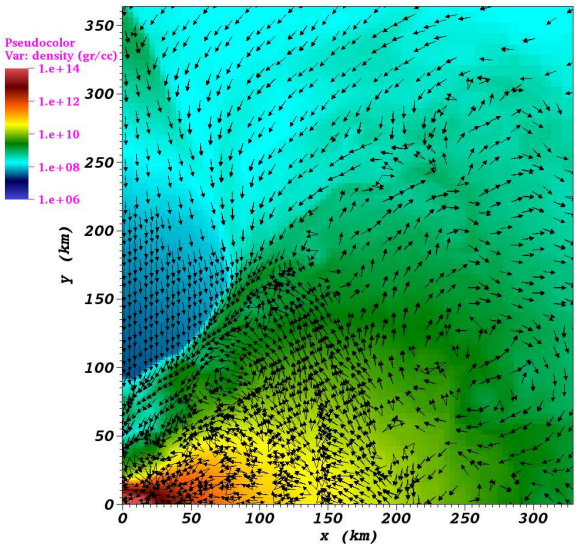

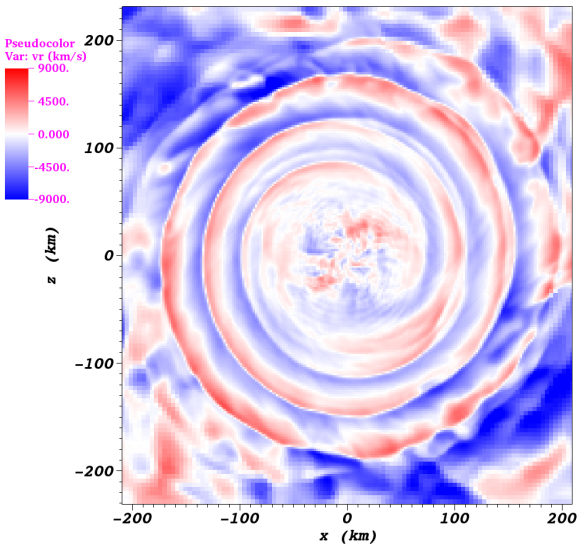

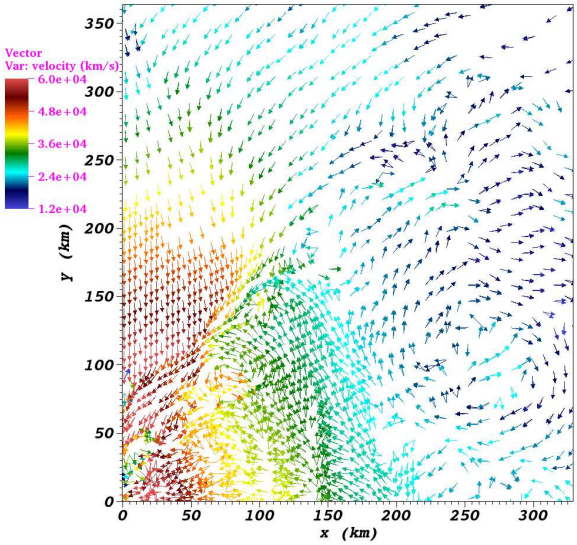

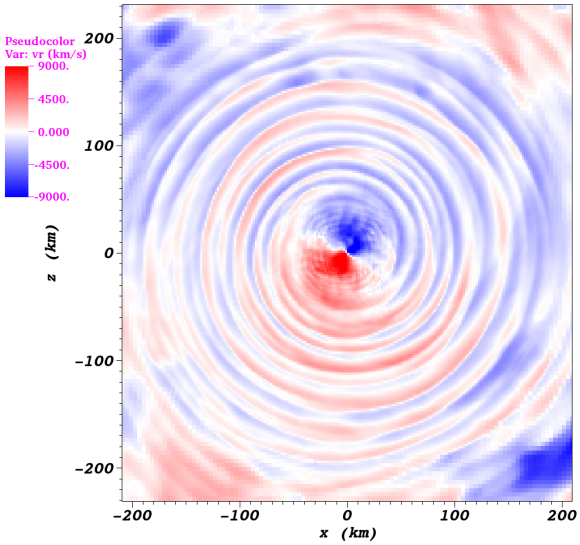

FIG. 4.— *Top:* Velocity flow field in the xy plane at $t_{\rm pb} = 224$ ms superimposed on top of the density color-map (close-up of the upper-right part of the central region of the lower-left panel in Fig. 3). *Bottom:* Velocity arrows color-coded according to the velocity magnitude, with the color-coding running from $v = 12000$ km s^{-1} to $v = 60000$ km s^{-1}. The development of large vortexes is clearly seen in this region.

FIG. 5.— Radial velocity in the equatorial (xz) plane of the star at two times after core bounce, $t_{\rm pb} = 104$ ms (top), and $t_{\rm pb} = 224$ ms (bottom). The color-coding runs from in-fall of $v_r = -9000$ km s^{-1} (blue) to outflow of $v_r = 9000$ km s^{-1} (red). The effective PNS radius calculated from its volume is $r_{\rm eff,PNS} \approx 75$ km, but as the PNS is highly oblate, the radius of its cross section in the xz plane is $r_{\rm eq,PNS} \approx 100$ km. The equatorial Keplerian velocity at its surface is $r_{\rm Kep,PNS} \approx 47500$ km s^{-1}.

tion of a millisecond magnetar which may later spin down and supply additional energy to the SN. The details of the spin evolution may be important for the energy available from magnetar spin down, and the initial asphericity of the PNS may produce gravitational waves (e.g., Camelio et al. 2016; Moriya & Tauris 2016). Still, for a magnetar to be relevant a successful SN explosion must first take place, otherwise the PNS will collapse into a BH early-on. This is in accordance to the proposal of Soker (2016) that jets accompany the formation of a magnetar.

Another consequence may be a rotationally-supported remnant NS exceeding the maximal possible mass for a non-rotating NS. The NS may later-on slow down and lose the rotational support, collapsing into a BH. This has been suggested by Falcke & Rezzolla (2014) as a possible mechanism for fast radio bursts.

3.4. *Neutron-rich disk*

Figure 10 shows the thick neutron-rich disk that forms around the PNS, where the electron to nucleon ratio, $Y_{\rm e}$, is relatively low. This is due to the increased weak interactions in regions of higher density (Fig. 3). In a thick disk-like structure with a height of several tens of kilometers, contain-

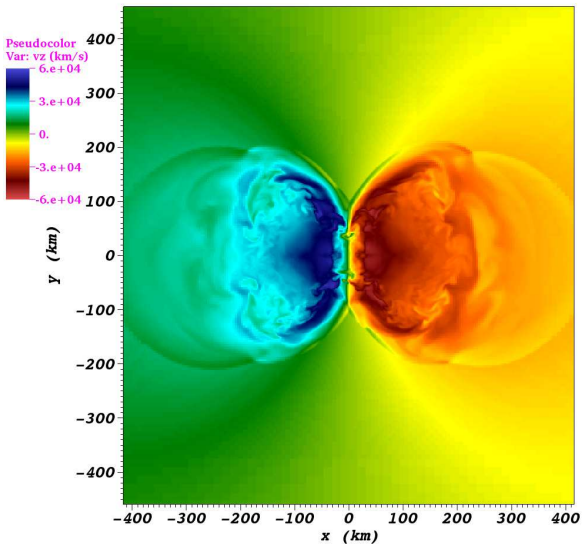

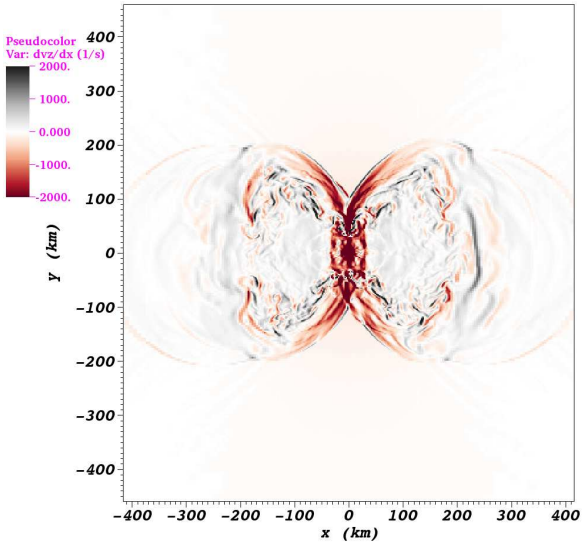

FIG. 6.— *Top:* Velocity perpendicular to the xy plane at $t_{\rm pb} = 104$ ms. There is a general counterclockwise rotation – blue hues represent material flow outwards from the paper, and red hues represent an inward motion (the z axis points outwards from the paper). *Bottom:* Derivative in the x direction of the velocity shown in the top panel, i.e., $\frac{\partial v_z}{\partial x}$ in units of s^{-1} and a scale given by the color-bar.

ing a mass of approximately $0.3 M_\odot$, this ratio reaches values of $Y_{\rm e} < 0.1$. Kohri et al. (2005) have previously suggested that rapid neutron capture (*r*-process) nucleosynthesis might take place due to winds from a neutron-rich disk, in the context of a wind-driven CCSN. If a successful explosion follows the collapse described in the simulation, as suggested in section 3.2, *r*-process elements will be ejected into the interstellar medium.

Many uncertainties still remain regarding the sites of *r*-process nucleosynthesis (Thielemann et al. 2011). This is in particular the case for the sites of strong *r*-process nucleosynthesis, where elements of atomic weight $A \geq 130$ are formed.

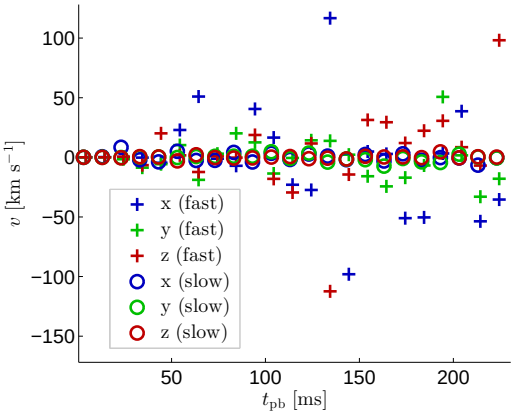

FIG. 7.— Average velocity of the PNS, defined as the region where the density is $\rho > 10^{11}$ g cm^{-3}, as function of time after core bounce for the rapidly-rotating progenitor (pluses) and for the slow rotator (circles).

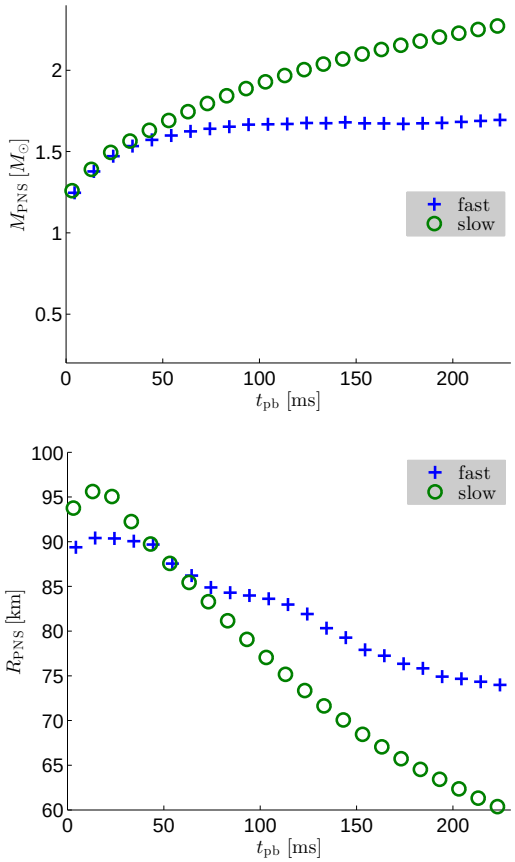

FIG. 8.— *Top:* PNS mass as function of time after core bounce for the rapidly-rotating progenitor (pluses) and for the slow rotator (circles), where the PNS is defined as the region where the density is $\rho > 10^{11}$ g cm^{-3}. *Bottom:* PNS effective radius ($\pi R_{\rm PNS}^3 = 0.75 V_{\rm PNS}$, where $V_{\rm PNS}$ is the PNS volume).

According to Wehmeyer et al. (2015), observed *r*-process elements are compatible with a combined origin of CCSNe from rapidly-rotating progenitors (e.g., Winteler et al. 2012; Nishimura et al. 2015) and NS mergers (e.g., Goriely et al. 2011; Hotokezaka et al. 2015; Wu et al. 2016). Further theoretical understanding will help in assessing the relative impor-

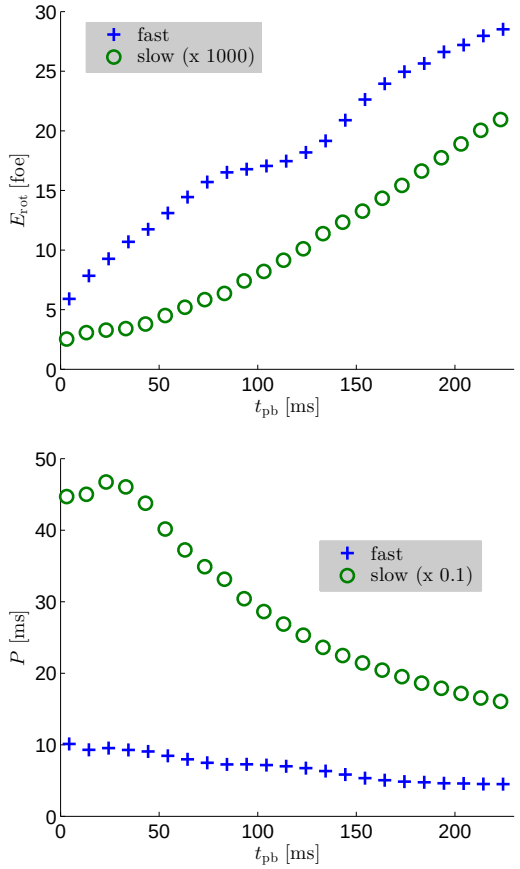

FIG. 9.— *Top:* Rotational kinetic energy of the PNS as function of time after core bounce for the rapidly-rotating progenitor (pluses) and for the slow rotator (circles). The energy of the slow rotator is multiplied by 10^3 for the presentation. *Bottom:* PNS spin period, where for the purpose of presentation the slow rotator period is multiplied by 0.1 .

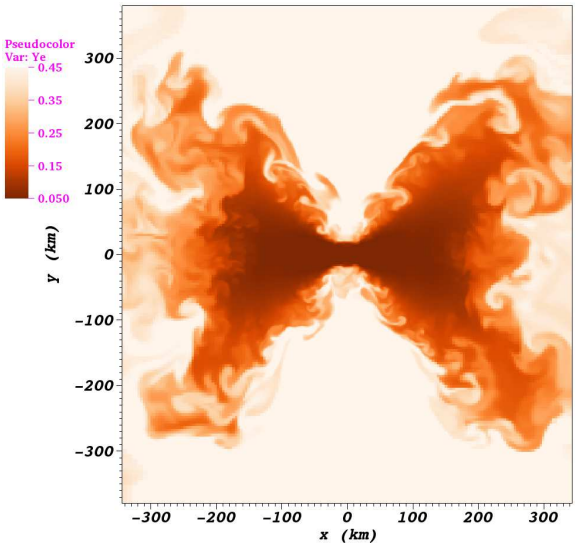

FIG. 10.— Color-map of electron fraction ($Y_{\rm e}$) in the xy plane at a post-bounce time of $t_{\rm pb} = 224$ ms. The color-coding runs from $Y_{\rm e} = 0.05$ (dark) to $Y_{\rm e} = 0.45$ (light).

tance of these two types of events, with the aid of observations such as the presence of heavy elements in stars of old dwarf galaxies (Ji et al. 2016). Papish et al. (2015) further raised the possibility that the strong *r*-process takes place in jets from a NS companion orbiting inside the core of a giant star. The simulation results reported in the present study strengthen the possible role of rotationally-dominated CCSNe in strong *r*-process nucleosynthesis. The extensive study of this issue is deferred to a future dedicated paper.

4. DISCUSSION AND SUMMARY

I have presented a study of important non-axisymmetric features in the collapse of a rapidly-rotating massive star, using the hydrodynamic code FLASH. I have used a rapidly-rotating progenitor star evolved with MESA excluding magnetic braking. This allowed for the straightforward comparison to a slowly-rotating case just by incorporation of the Spruit dynamo. In future studies, more realistic progenitors resulting from binary interactions should be used.

Massive stars with high core rotation rates, as in the progenitor model used in this study, may be relatively rare as they need strong binary interaction to acquire their angular momentum. The collapse and possible explosion of such stars can still be significant in explaining some observed phenomena. A prolonged bipolar outflow, as suggested in section 3.2, can function as the engine of extremely energetic SNe. This agrees with the elongated morphology implied by recent observations (Inserra et al. 2016). Asymmetric momentum distribution (section 3.3) can give birth to BHs with significant natal kicks. The neutron-rich disk discussed in section 3.4 can induce strong *r*-process nucleosynthesis of heavy elements.

The rapidly-rotating PNS formed in the simulation can be an early-stage millisecond magnetar, which may later deposit a large amount of energy in the SN ejecta during its spin-down. First, an explosion must take place. It is unlikely to be driven by the neutrino flux, so a jet-driven SN might be more promising. Estimating the quantitative energy contributions of the jets and the magnetar requires further study, yet it seems the energy available should suffice for SLSNe. I suggest that Type I SLSNe result from flow dynamics qualitatively similar to the presented simulation, and also contribute to the production of strong *r*-process elements.

ACKNOWLEDGMENTS

I thank Noam Soker for his guidance and for fruitful discussions. The software used in this work was developed in part by the DOE NNSA-ASC and DOE Office of Science ASCR-supported Flash Center for Computational Science at the University of Chicago. Simulations were run on the Israeli astrophysics I-CORE astric HPC.

REFERENCES

Angus C. R., Levan A. J., Perley D. A., Tanvir N. R., Lyman J. D., Stanway E. R., Fruchter A. S., 2016, MNRAS, 458, 84
Blondin J. M., Mezzacappa A., 2007, Nature, 445, 58
Blondin J. M., Mezzacappa A., DeMarino C., 2003, ApJ, 584, 971
Bray J. C., Eldridge J. J., 2016, MNRAS, tmp, 933
Camelio G., Gualtieri L., Pons J. A., Ferrari V., 2016, Phys. Rev. D, 94, 024008
Cantiello M., Yoon S. C., Langer N., Livio M., 2007, A&A, 465, L29
Chatzopoulos E., Wheeler J. C., 2012, ApJ, 760, 154
Chatzopoulos E., Wheeler J. C., Vinko J., Nagy A. P., Wiggins B. K., Even W. P., 2016, arXiv:1603.06926
Chen K. J., Woosley S. E., Sukhbold, T., 2016, arXiv:1604.07989
Couch S. M., O'Connor E. P., 2014, ApJ, 785, 123
Couch S. M., Graziani C., Flocke N., 2013, ApJ, 778, 181
de Mink S. E., Langer N., Izzard R. G., Sana H., de Koter A., 2013, ApJ, 764, 166
Dexter J., Kasen D., 2013, ApJ, 772, 30
Dong S. et al., 2016, Science, 351, 257
Drout M. R. et al., 2011, ApJ, 741, 97
Falcke H., Rezzolla L., 2014, A&A, 562, 137
Fernández R., 2010, ApJ, 725, 1563
Fryer C. L., Heger A., 2005, ApJ, 623, 302
Fryxell B. et al., 2000, ApJS, 131, 273
Gal-Yam A., 2012, Science, 337, 927
Gilkis A., Soker N., Papish O., 2016, ApJ, 826, 178
Goriely S., Bauswein A., Janka H.-T., 2011, ApJ, 738, L32
Hotokezaka K., Piran T., Paul M., 2015, Nature Physics, 11, 1042
Inserra C. et al., 2013, ApJ, 770, 128
Inserra C., Bulla M., Sim S. A., Smartt S. J., 2016, arXiv:1607.02353
Iwakami W., Kotake K., Ohnishi N., Yamada S., Sawada K., 2009, ApJ, 700, 232
Izzard R. G., Ramirez-Ruiz E., Tout C. A., 2004, MNRAS, 348, 1215
Janka H.-T., 2012, Annual Review of Nuclear and Particle Science, 62, 407
Janka H.-T., 2013, MNRAS, 434, 1355
Janka H.-T., Melson T., Summa A., 2016, arXiv:1602.05576
Ji A. P., Frebel A., Chiti A., Simon J. D., 2016, Nature, 531, 610
Kasen D., Bildsten L., 2010, ApJ, 717, 245
Kasen D., Woosley S. E., 2009, ApJ, 703, 2205
Kasen D., Metzger B. D., Bildsten L., 2016, ApJ, 821, 36
Kohri K., Narayan R., Piran T., 2005, ApJ, 629, 341
Kuroda T., Takiwaki T., Kotake K., 2014, Phys. Rev. D, 89, 044011
Kuroda T., Takiwaki T., Kotake K., 2016, ApJS, 222, 20
Langer N., 2012, ARA&A, 50, 107
Lattimer J. M., Swesty F. D., 1991, NuPhA, 535, 331
Leloudas G. et al., 2015, MNRAS, 449, 917
Lentz E. J. et al., 2015, ApJ, 807, L31
Liebendörfer M., 2005, ApJ, 633, 1042
Lunnan R. et al., 2014, ApJ, 787, 138
Mandel I., 2016, MNRAS, 456, 578
Mandel I., de Mink S. E., 2016, MNRAS, 458, 2634
Martins F., Depagne E., Russeil D., Mahy L., 2013, A&A, 554, 23
Masada Y., Takiwaki T., Kotake K., 2015, ApJ, 798, L22
Mcley L., Soker N., 2014, MNRAS, 445, 2492
Melson T., Janka H.-T., Marek A., 2015, ApJ, 801, L24
Metzger B. D., Margalit B., Kasen D., Quataert E., 2015, MNRAS, 454, 3311
Meynet G., Maeder A., 2000, A&A, 361, 101
Milosavljević M., Lindner C. C., Shen R., Kumar P., 2012, ApJ, 744, 103
Mösta P. et al., 2014, ApJ, 785, L29
Mösta P., Ott C. D., Radice D., Roberts L. F., Schnetter E., Haas R., 2015, Nature, 528, 376
Moriya T. J., Tauris T. M., 2016, MNRAS, 460, L55
Müller B., 2016, arXiv:1608.03274
Nakamura K., Kuroda T., Takiwaki T., Kotake K., 2014, ApJ, 793, 45
Nishimura N., Takiwaki T., Thielemann F.-K., 2015, ApJ, 810, 109
Nugis T., Lamers H. J. G. L. M., 2000, A&A, 360, 227
O'Connor E., Ott C. D., 2010, Class. Quantum Grav., 27, 11410
Ofek E. O. et al., 2007, ApJ, 659, L13
Ouyed R., Leahy D., Koning, N., 2015, MNRAS, 454, 2353
Ouyed R., Leahy D., Koning, N., 2016, ApJ, 818, 77
Ott C. D., Dimmelmeier H., Marek A., Janka H.-T., Hawke I., Zink B., Schnetter E. 2007, Phys. Rev. Lett., 98, 261101
Ott C. D. et al., 2013, ApJ, 768, 115
Papish O., Soker N., Bukay I., 2015, MNRAS, 449, 288
Paxton B. et al., 2011, ApJS, 192, 3
Paxton B. et al., 2013, ApJS, 208, 4
Paxton B. et al., 2015, ApJS, 220, 15
Podsiadlowski P., Mazzali P. A., Nomoto K., Lazzati D., Cappellaro E., 2004, ApJ, 607, L17
Prajs S. et al., 2016, arXiv:1605.05250
Quataert E., Shiode J., 2012, MNRAS, 423, L92
Quimby R. M. et al., 2011, Nature, 474, 487
Quimby R. M., Yuan F., Akerlof C., Wheeler J. C., 2013, MNRAS, 431, 912
Rembiasz T., Guilet J., Obergaulinger M., Cerdá-Durán P., Aloy M. A., Müller E., 2016, MNRAS, tmp, 888
Repetto S., Nelemans G., 2015, MNRAS, 453, 3341
Repetto S., Davies M. B., Sigurdsson S., 2012, MNRAS, 425, 2799
Rest A. et al., 2011, ApJ, 729, 88
Roberts L. F., Ott C. D., Haas R., O'Connor E. P., Diener P., Schnetter E., 2016, arXiv:1604.07848
Sanders N. E. et al., 2012, ApJ, 756, 184
Shiode J. H., Quataert E., 2014, ApJ, 780, 96
Soker N., 2016, NewA, 47, 88
Soker N., Gilkis A., 2016, arXiv:1606.06544
Song H. F., Meynet G., Maeder A., Ekström S., Eggenberger P., 2016, A&A, 585, 120
Spruit H. C., 2002, A&A, 381, 923
Sukhbold T., Woosley S. E., 2016, ApJ, 820, L38
Takiwaki T., Kotake K., Suwa Y., 2016, MNRAS, 461, L112
Thielemann F.-K. et al., 2011, PrPNP, 66, 346
Vink J. S., de Koter A., Lamers H. J. G. L. M., 2001, A&A, 369, 574
Wehmeyer B., Pignatari M., Thielemann F.-K., 2015, MNRAS, 452, 1970
Winteler C., Käppeli R., Perego A., Arcones A., Vasset N., Nishimura N., Liebendörfer M., Thielemann F.-K., 2012, ApJ, 750, L22
Woosley S. E., Heger A., 2006, ApJ, 637, 914
Wu M.-R., Fernández R., Martínez-Pinedo G., Metzger B. D., 2016, arXiv:1607.05290
Yoon S.-C., Langer N., 2005, A&A, 443, 643
Yoon S.-C., Woosley S. E., Langer N., 2010, ApJ, 725, 940